Thermal conduction in a densified oxide glass

Insights from lattice dynamics

Sørensen, Søren Strandskov; Cielecki, Pawel Piotr; Johra, Hicham; Bockowski, Michal; Skovsen, Esben; Yue, Yuanzheng; Smedskjær, Morten Mattrup

Published in:
Materials Today Communications

DOI (link to publication from Publisher):
10.1016/j.mtcomm.2022.104160

Publication date:
2022

Document Version
Publisher's PDF, also known as Version of record

Materials Today Communications 32 (2022) 104160

Contents lists available at ScienceDirect

Materials Today Communications

journal homepage: www.elsevier.com/locate/mtcomm

Thermal conduction in a densified oxide glass: Insights from lattice dynamics

Søren S. Sørensen [a], Paweł P. Cielecki [b], Hicham Johra [c], Michal Bockowski [d], Esben Skovsen [b], Yuanzheng Yue [a], Morten M. Smedskjaer [a,*]

[a] Department of Chemistry and Bioscience, Aalborg University, DK-9220 Aalborg, Denmark
[b] Department of Materials and Production, Aalborg University, DK-9220 Aalborg, Denmark
[c] Department of the Built Environment, Aalborg University, DK-9220 Aalborg, Denmark
[d] Institute of High-Pressure Physics, Polish Academy of Sciences, 01–142 Warsaw, Poland

ARTICLE INFO

Keywords:
Thermal conductivity
Modified oxide glass
Pressure
Densification
Molecular dynamics
Lattice dynamics

ABSTRACT

Thermal conductivity is an important property of oxide glasses, but its structural origins remain largely unknown. Here, we provide detailed modal information on thermal conductivity in a calcium aluminosilicate glass by relying on recent advances in lattice dynamics methods. We probe various structural features using molecular dynamics simulations by densifying the glass at pressures up to 100 GPa and studying the vibrational, mechanical, and thermal properties. We demonstrate good agreement between these simulations and complementary experiments, both of which indicate significant pressure-induced alteration of mechanical moduli, vibrational density of states, boson peak behavior, and thermal conductivity. We also find an intriguing correlation between the boson peak frequency and the total thermal conductivity in both the current glass series and a lithium borate glass series reported in literature. This correlation scales with the Debye frequency, suggesting that both parameters are associated with the transformation of the elastic medium under pressure.

1. Introduction

The thermal conductivity of amorphous materials is very challenging to theoretically describe due to both their lack of long-range order and the related complex mixture of modal contributions to heat transfer [1]. While the traditional phonon gas model [2] has provided new insight into the nature of heat conduction in glasses [3], it lacks predictivity and is fundamentally flawed in describing the modal behavior of heat transfer in glasses, especially with respect to modes not resembling the classical 'phonon'-picture [4–6]. Allen and Feldman introduced a model to quantify the contribution of "diffusive" modes to heat transfer based on a harmonic lattice dynamical description [7,8]. These diffusive modes are non-propagative ("non-phononic") as characterized by their eigenvectors and generally provide a relatively low modal contribution to thermal conductivity. As such, the total contribution of so-called diffusons is often taken as a lower limit of thermal conductivity [9], in similarity to simpler models of such lower limits of thermal conductivity [10,11]. Recently, the phonon gas model and the diffusive regime described by Allen and Feldman have been proposed as the anharmonic and harmonic limits of a lattice dynamical derivation, respectively [12,13]. This has enabled a unified description of the thermal conduction in systems exhibiting significant contributions from both propagative and diffusive heat transfer regimes. Furthermore, the result enables the study of modal characteristics of amorphous materials for which traditional methods based on simulations and lattice dynamics break down due to the lack of lattice periodicity[14]. While there has been some interest in the literature in the various methods for accessing modal thermal conductivity, most studies (with a notable exception on cementitious phases [15]) have focused on compositionally simple systems such as amorphous silicon and amorphous SiO_2 [7,16]. These studies have provided novel insights into the studied systems, but they neglect the role of more complex structural and topological features that are present in systems with mixed network formers and network modifiers. Here, network formers are those oxides that form the ionocovalent backbone structure of the glass (e.g., SiO_2, B_2O_3, GeO_2), while network modifiers are those that form more ionic bonds and rupture the network (e.g., alkali and alkaline earth oxides) [17,18].

To broaden the understanding of heat transfer beyond that in the

* Corresponding author.
E-mail address: mos@bio.aau.dk (M.M. Smedskjaer).

https://doi.org/10.1016/j.mtcomm.2022.104160
Received 15 June 2022; Received in revised form 1 July 2022; Accepted 1 August 2022
Available online 3 August 2022

simplest oxides and to provide the first test of the recent advances within lattice dynamics on oxide glasses, we here probe a ternary calcium aluminosilicate glass of composition $30CaO\text{-}10Al_2O_3\text{-}60SiO_2$ (CAS) using both molecular dynamics (MD) simulations and experiments. We densify the CAS glasses to obtain a diverse range of structural features with significant changes in both short- and medium-range order structure. We note that CAS glasses are of interest in both industrial [19,20] and fundamental glass science [21,22] as well as geology [23] due the abundance of the chemical constituents in Earth's crust. Furthermore, this glass composition has a wide range of structural features due to the modifying role of CaO, the network intermediate role of Al_2O_3 (i.e., Al_2O_3 can act as either network former or modifier, depending on the molar ratio between them and in turn the coordination number of Al), as well as the network forming role of SiO_2 [18,23]. Using the well-tested Matsui potential for classical MD simulations [24], we rely on recent advances in lattice dynamics to probe the vibrational characteristics, e.g., the full and partial vibrational density of states, the boson peak, participation ratio, and the anharmonic modal thermal conductivity. Based on these results, we find a striking coupling between the boson peak frequency and thermal conductivity. We supplement the simulations with experiments of hot-compressed glasses to confirm similar behavior of thermal conductivity and boson peak as found in simulations.

2. Methods

2.1. MD simulations

Glasses of composition $30CaO\text{-}10Al_2O_3\text{-}60SiO_2$ were prepared following a typical melt-quenching procedure using the LAMMPS software [25] and the interatomic potential parameters of Matsui [24]. We employed a gradient cutoff of the coulombic interactions using the Wolf method. First, we placed 493 atoms (51 Ca, 306 O, 34 Al, 102 Si) randomly in a simulation box with a minimum separation of 1.8 Å. The latter restriction was employed to avoid unphysical initial overlap of atoms. Next, an energy minimization was performed before initiating dynamics at pressures of 0–100 GPa (with 10 GPa intervals) at a temperature of 5000 K in the *NPT* ensemble, except in the case of 0 GPa pressure where dynamics were initiated using 1 GPa of hydrostatic pressure to avoid volatilization of the simulation box. The liquid was then relaxed for 1 ns before cooling it down to 300 K at 1 K ps^{-1}, except in the 0 GPa case where pressure was relieved from 1 GPa to 0 GPa during the initial cooling from 5000 to 4000 K. Finally, the system was kept under the designated pressure for another 1 ns to allow for relaxation, before performing 100 ps of statistical averaging in the *NVT* ensemble. Now, the coordination numbers of the atoms were determined by counting the numbers of atoms within the first coordination shell based on the partial radial distribution functions. It was found that a generic cutoff of 2.2 Å was meaningful for all glasses and studied interactions.

The elastic constants of the simulated systems were estimated by measuring the directional pressures while deforming the minimized simulation box in the *xx*, *yy*, *zz*, *xy*, *xz*, and *yz* directions using strain steps of 0.001 and 0.1 for tensile and shear strain, respectively. Linear regression of the elastic region then yielded the C_{11} and C_{44} elastic constants. These were used to estimate the Young's (E), shear (G), and bulk (B) moduli as well as the Poisson's ratio (ν), as,

$$C_{12} = C_{11} - 2C_{44}, \tag{1}$$

$$E = \frac{(C_{11} - C_{12})(C_{11} + 2C_{12})}{C_{11} + C_{12}}, \tag{2}$$

$$G = C_{44}, \tag{3}$$

$$B = \frac{C_{11} + 2C_{12}}{3}, \tag{4}$$

$$\nu = \frac{C_{12}}{C_{11} + C_{12}}. \tag{5}$$

Thermal and vibrational properties were obtained through second and third-order force constant evaluation and analyses. Specifically, the structures obtained from quenching and relaxation were subjected to an energy minimization. Subsequently, LAMMPS was employed to calculate second and third order force constants through the finite displacement method. No cutoff, besides that given by the interatomic potential, was employed. Then, second order force constants (ϕ_{ij}) were used to determine the full dynamical matrix (**D**), which can be exploited to acquire the eigenfrequencies (Ω) and eigenvectors (**e**) of the system by solving [26],

$$\mathbf{e}\cdot\Omega = \mathbf{D}\cdot\mathbf{e}, \tag{6}$$

where **e** is a matrix providing the atomic motion related to each eigenmode and Ω is a square matrix with a diagonal of squared eigenfrequencies (ω^2). Based on Ω, we calculated the vibrational density of states ($g(\omega)$) by binning into a histogram as,

$$g(\omega) = \sum_{i}^{3N} \delta(\omega_i - \omega), \tag{7}$$

where δ is the Dirac delta and N is the number of atoms in the system. To provide an estimation of the boson peak based on $g(\omega)$, the reduced vibrational density of states ($g(\omega)\omega^{-2}$) was calculated by fitting an 8th degree polynomial to the low-frequency part (~0–20 THz) of $g(\omega)$ and transforming the fitted curve by $g(\omega)\omega^{-2}$. This was done to avoid low frequency noise in the data and allow for an analytical solution of the boson peak frequency (ω_{BP}).

Next, the participation ratio (PR) of the ith mode was determined based on the nth atomic displacement vector of each ith mode, $\overline{e}_{n,i}$, and calculated as,

$$PR_i = \left(N \sum_{n}^{N} \left|\overline{e}_{n,i}\right|^4\right)^{-1} \tag{8}$$

This was done to estimate the degree of participation of atoms for each mode. Similarly, we estimated the degree of participation of each atomic species by exploiting the normalization of the eigenvectors for each mode,

$$\sum_{n}^{N} \overline{e}_{n,i}\cdot\overline{e}_{n,i} = \sum_{n}^{N_O} \overline{e}_{n,i}\cdot\overline{e}_{n,i} + \sum_{n}^{N_{Si}} \overline{e}_{n,i}\cdot\overline{e}_{n,i} + \sum_{n}^{N_{Al}} \overline{e}_{n,i}\cdot\overline{e}_{n,i} + \sum_{n}^{N_{Ca}} \overline{e}_{n,i}\cdot\overline{e}_{n,i} = 1. \tag{9}$$

Subsequently, this was exploited to provide a weight of the vibrational contribution of each atomic species by calculating the individual sums of Eq. 9. We denote the sums $w_{O/Si/Al/Ca}$, and refer to this parameter as the mode weight. The mode weights are used to access the partial $g(\omega)$[27].

Finally, to estimate the thermal conductivity of the simulated glasses, we used the recently developed quasi-harmonic Green Kubo (QHGK) method [12,28] through the kALDo software. [13] The method represents a unification of the diffusive contribution to thermal conductivity as described by Allen and Feldman [7] and that of propagative behavior of the phonon gas model [2], providing per-mode thermal conductivity estimations. Practically, the second and third order force constants were calculated using LAMMPS before being imported into kALDo. All estimations in kALDo were performed using a specified temperature of 300 K and quantum statistics.

2.2. Experiments

The $30CaO\text{-}10Al_2O_3\text{-}60SiO_2$ glass was prepared by the traditional melt-quenching method. That is, raw materials of $CaCO_3$, Al_2O_3, and SiO_2 were mixed in a Pt90Rh10 crucible and homogenized at around 1650 °C for several hours. Then, the sample was quenched onto a metal

plate and subsequently annealed at T_g (769 °C) for ~30 min. Hot-compression experiments were performed in accordance with previous work [29,30] by heating to T_g under 1 GPa of N_2 gas pressure, maintaining the pressure for 30 min, followed by cooling to room temperature and subsequent decompression.

Density of glasses (ρ) were measured using the Archimedes' method by measuring the sample mass in air (m_{air}) and when submerged in absolute ethanol (m_{sub}) by,

$$\rho = \frac{\rho_{EtOH} m_{air}}{m_{air} - m_{sub}}, \quad (10)$$

where the density of absolute ethanol is $\rho_{EtOH} = 0.7871$ g cm^{-3}.

Differential scanning calorimetry (DSC) was used to measure the glass transition temperature (T_g) of the produced CAS glass using the approach described elsewhere [31] by heating it at 10 K min^{-1} in an argon atmosphere. The isobaric heat capacities (C_p) of annealed and hot-compressed glasses were obtained by comparing the baseline-corrected heat flow curves of the samples with those of a reference sapphire sample. Afterwards, C_p vs. T data below T_g were fitted to the Maier-Kelley equation [32],

$$C_p(T) = a + bT - cT^{-2} \quad (11)$$

This fitting allowed us to extrapolate the C_p data to room temperature (300 K).

Thermal diffusivity (α) measurements were conducted with the laser flash method using a Netzsch LFA 447 instrument with disc-shaped samples of ~6 mm in diameter and thickness of ~1 mm. The experimental procedure follows that of Ref. [33]. Ultimately, thermal conductivity (κ) at room temperature was determined by combining the ρ, α and C_p data,

$$\kappa = \alpha C_p \rho. \quad (12)$$

Terahertz time-domain spectroscopy (THz-TDS) was performed using a commercial THz spectrometer (TeraSmart, Menlo Systems), where the THz pulses from a photoconductive antenna (PCA) were collimated, focused onto the sample, recollimated and focused onto a PCA detector using a series of four TPX lenses. The full THz path was enclosed in a custom-made purge chamber that was purged by dry nitrogen to remove water vapor. The purge chamber was designed to have a very small volume to allow fast purging of the chamber after switching samples [34]. Samples (cylinders of ~0.5 mm thickness polished to an optical finish) were fixed in a sample holder with a clear aperture larger than the spot size of the focused THz beam. After purging with N_2 for a few minutes, time-domain spectra were averaged over 1000 scans, each covering 150 ps. Reference spectra were collected in a similar manner using the same sample holder, but without a sample. Data analyses were performed in the as-supplied software by restricting the interval of the time domain signal to avoid the time range of the internal echo of the sample. Obtained absorption coefficients as a function of frequency were smoothened by the LOWESS algorithm.

3. Results and discussion

The pressure dependence of density (ρ) strongly depends on the material chemistry. For the studied CAS glass system, the MD-simulated pressure dependence of ρ is presented in Fig. 1. Here, the density is found to increase in different regimes, i.e., first rather steeply from 0 to 20 GPa and then at a lower rate above 20 GPa, ultimately approaching a value of ~5 g cm^{-3} at 100 GPa. This is in good agreement with the experimental value of 2.73 g cm^{-3}, which increases to 2.78 g cm^{-3} after hot-compression at 1 GPa of N_2 pressure (see Table S1). Interestingly, comparing the initial density dependences on pressure detected by both simulations (comparing the 0 and 10 GPa samples) and experiments, we find a rate of increase in ρ with pressure of 0.065 g cm^{-3} GPa^{-1}, which is similar to that found in other oxide glass systems[30,33].

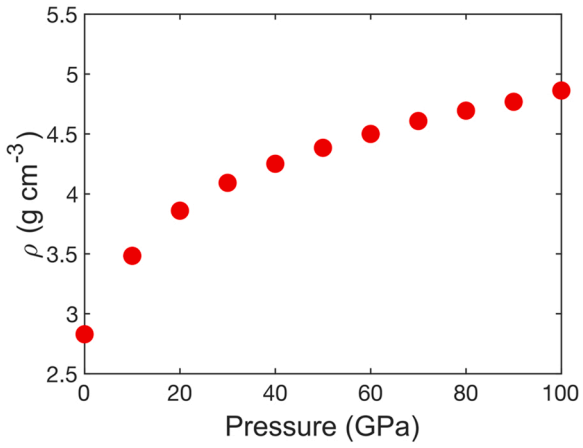

Fig. 1. Density (ρ) as function of pressure for the simulated 30CaO-10Al_2O_3-60SiO_2 glasses.

Fig. 2 shows the pressure dependence of the coordination number (CN) for silicon, aluminum, and oxygen for all simulated glasses. For all three atomic species, CN increases with increasing pressure. The CNs of both silicon and aluminum increase from 4 to ~5.7 when increasing the pressure from 0 G to 100 GPa. A smaller pressure (<10 GPa) is required for CN alteration of Al to be initiated than that of Si (around 10–20 GPa). These differences are in good agreement with those in pressure response of Al and Si in a range of calcium aluminates and calcium aluminosilicate glasses studied by both in situ cold compression and *ex situ* compression [35] as well as the expectation of CN changes of feldspar crystals under pressure [36]. We note that the maximum CN of ~5.7 for both Si and Al is not directly comparable to that of experimental glasses, which would likely approach a CN value of 6 even at pressures below 100 GPa of hydrostatic pressure. For oxygen, the average CN increases from ~1.8 (due to the presence of non-bridging oxygens) to ~2.5 upon compression, which is in good agreement with the general expectation for silicates [37].

A more detailed characterization of glass structure beyond CNs is provided by various scattering functions, e.g., the structure factor ($S(Q)$). The neutron-weighted $S(Q)$ of the 0 GPa simulated 30CaO-10Al_2O_3-60SiO_2 glass as well as that of comparable experimental

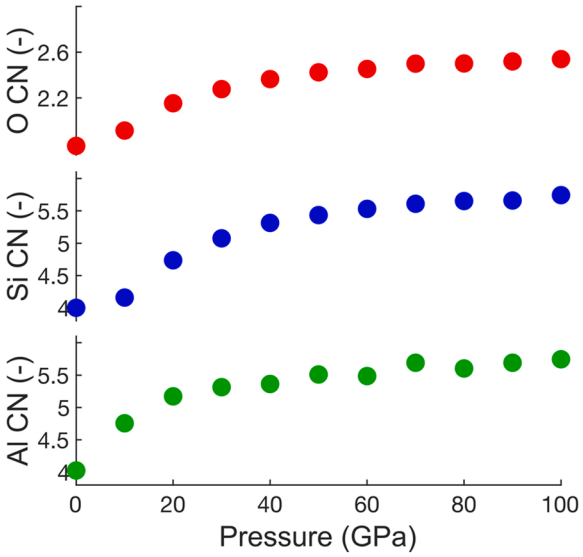

Fig. 2. Coordination numbers (CNs) of oxygen (red), silicon (blue), and aluminum (green) as a function of pressure for the simulated 30CaO-10Al_2O_3-60SiO_2 glasses.

neutron scattering data from literature [38,39] are presented in Fig. 3a. Very good agreement between the simulated and experimental $S(Q)$ is observed, although minor shifting in peak positions and mismatching of a few peak intensities is noted. This confirms that the MD simulations replicate atomic structure at both the short- and medium-range order length scales well, in agreement with previous simulations of the uncompressed glass using the Matsui potential [22]. The computed $S(Q)$s for all simulated CAS samples are presented in Fig. 3b. The first sharp diffraction peak for the 0 GPa glass (at Q~2 Å^{-1}) gradually decreases in intensity and shifts to higher Q values with increasing pressure, and finally vanishes. This pressure-induced peak shift to higher Q is also seen for the other peaks in the spectra, meaning that all the peaks shift to shorter distances in real space [40], i.e., a more compact atomic structure is realized. This trend is in good agreement with the increase in density (Fig. 1). The corresponding radial distribution function associated with the presented $S(Q)$ of Fig. 3b are presented in Fig. S1, showing a pressure-induced broadening and increase in distance of the peak at lowest separation. This change ultimately represents the CN changes of Fig. 2. Moreover, the correlations at longer distances show significant decrease in distance, as expected for structural densification.

To further confirm the ability of the MD simulations to reproduce the CAS glass structure and properties, we have also evaluated the elastic properties. Table 1 shows a comparison of the simulated and experimental Young's (E), shear (G), and bulk (B) moduli as well as the Poisson's ratio (ν) of the as-prepared glass. These simulated mechanical properties are generally in fair agreement with experimental values[41].

Next, we present the simulated mechanical properties of the densified glasses in Fig. 4. For the elastic moduli (Fig. 4a), we find an approximate linear increase in E, G, and B with pressure, reaching values of 470 GPa, 170 GPa, and 650 GPa for E, G, and B, respectively, at a pressure of 100 GPa. For the Poisson's ratio (Fig. 4b), we see a sharp increase from 0.28 for the as-prepared glass to a nearly constant value of ~0.37 for glasses compressed at pressures of $\geq$ 10 GPa.

Closely related to the elastic moduli are the longitudinal and transversal sound speeds, shown in Fig. 5. The transversal sound speed exhibits an increase with increasing pressure from ~3100 m s^{-1} for the as-prepared glass to ~5900 m s^{-1} for the glass compressed at 100 GPa, while the longitudinal sound speed increases from ~5700 m s^{-1} to ~13400 m s^{-1} in the same pressure range. Both glasses exhibit a change in the pressure dependence of sound speed in the range of around 20–30 GPa, with a smaller pressure-induced increase at higher pressures. We are not aware of any direct experimental measurements that would be comparable for the studied CAS glass. However, we note that previous measurements on magnesium silicate and aluminosilicate glasses under compression [42,43] show longitudinal and transversal sound speeds in a similar range as that found for the present CAS glasses.

Table 1
Simulated and experimental Young's (E), shear (G), and bulk (B) moduli, as well as the Poisson's ratio (ν) of the 30CaO-10Al_2O_3-60SiO_2 glass. Experimental values are from Ref.[41]. Errors of E, G, B, and ν from simulations are estimated to be 7.4 GPa, 3.2 GPa, 9.1 GPa, and 0.04, respectively.

	Simulated	Experimental (Ref.[41])
E (GPa)	70.9	93.3
G (GPa)	27.7	35.9
B (GPa)	55.4	77.5
ν (-)	0.28	0.30

Now, to understand the vibrational properties of the as-prepared and compressed simulated CAS glasses, we compute the second order force constants (see Section 2), from which the vibrational density of states ($g(\omega)$, where ω denotes frequency) can be determined. Fig. 6a shows an experimental $g(\omega)$ for an as-prepared 43CaO-14Al_2O_3-43SiO_2 glass as measured by neutron scattering [44] (dashed line) as well as the calculated $g(\omega)$ from simulations. It is seen that a good agreement between the simulated 0 GPa pressure sample (red line) and the experimental $g(\omega)$ is achieved [44], i.e., a sharp band at lower frequencies (0–20 THz) is found and accompanied by the presence of a higher frequency band (~30 THz). Interestingly, at higher pressures, the two bands of the $g(\omega)$ appear to merge and decrease in intensity. Considering the partial contributions of atoms to $g(\omega)$ that are calculated by multiplying the total $g(\omega)$ with the mode weights from Eq. (9) (see Figs. S2a-d), we find that oxygen, silicon, and partially aluminum have contributions in the full spectral width, while calcium mainly has contributions at $<$ 20 THz. Most notably, oxygen has by far the largest contribution to $g(\omega)$.

In Fig. 6b, we consider the pressure dependence of the boson peak (BP), which is a vibrational feature commonly found in disordered systems as an excess of vibrational states above the Debye level. To this end, we fit an analytical function (8th degree polynomial) to the lower frequency part (0–20 THz) of the curve in Fig. 6a and then transform it into the "reduced" vibrational density of states, i.e., $g(\omega)\omega^{-2}$, as shown in Fig. 6b. Such transformation is performed to make the Debye level a straight horizontal line in the plot. We perform such fitting as the fluctuations in the $g(\omega)$ of Fig. 6a would otherwise have been significantly enlarged due to the ω^{-2} factor and hence provide error in the estimation of the BP frequency. As shown in Fig. 6b, we find a pronounced BP peak in all simulated glasses, with a decreasing intensity and increasing frequency of the BP (ω_{BP}) with increasing pressure (see also Fig. 6c).

Experimentally THz time-domain spectroscopy measurements on the hot-compressed glasses show a pronounced BP (inset in Fig. 6b), with ω_{BP} found to be very similar to that observed in the simulations (for the

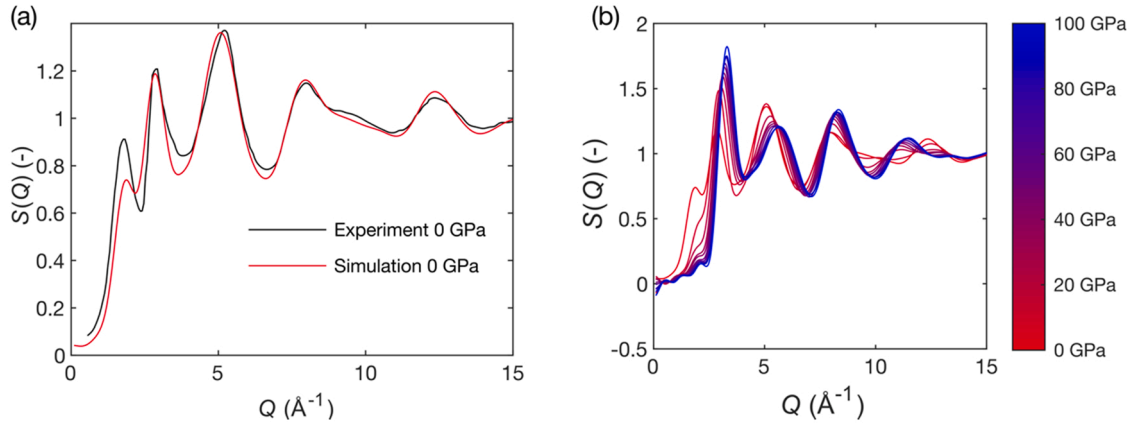

Fig. 3. (a) Calculated neutron-weighted structure factor ($S(Q)$) of the 30CaO-10Al_2O_3-60SiO_2 glass simulated at 0 GPa of pressure (red) as well as literature measurements on the same composition from neutron scattering (black) [38,39]. (b) Neutron-weighted structure factors of the simulated 30CaO-10Al_2O_3-60SiO_2 glasses that have been compressed from 0 to 100 GPa of pressure. Color indicates pressure from 0 GPa (red) to 100 GPa (blue) as indicated on the color bar.

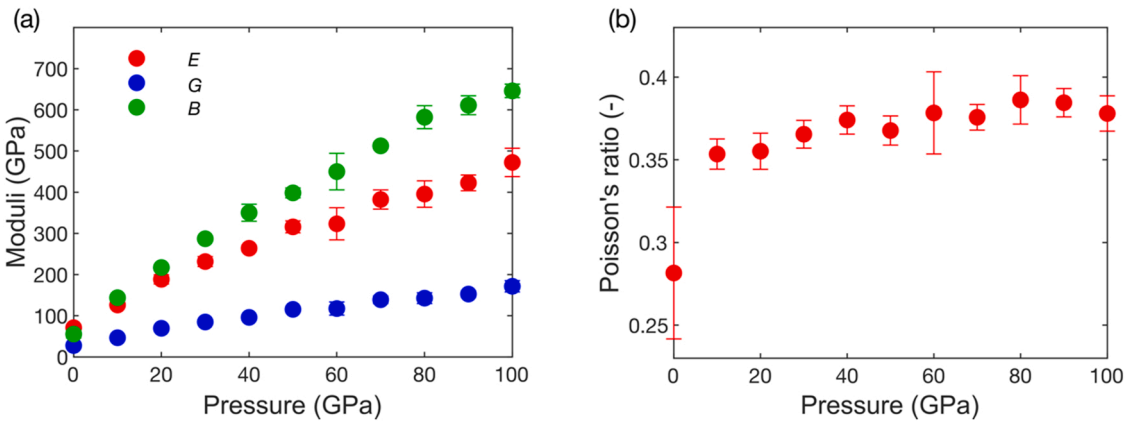

Fig. 4. (a) Pressure dependences of Young's (*E*, red), shear (*G*, blue), and bulk (*B*, green) moduli as well as (b) Poisson's ratio of the simulated 30CaO-10Al_2O_3-60SiO_2 glasses from 0 to 100 GPa of hydrostatic pressure.

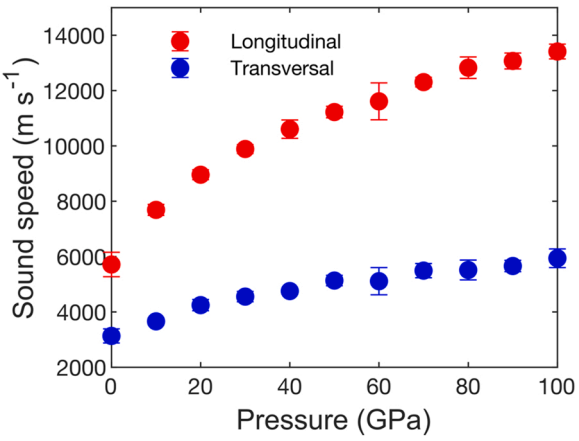

Fig. 5. Longitudinal (red) and transversal (blue) sound speed of the simulated 30CaO-10Al_2O_3-60SiO_2 glasses as a function of pressure.

as prepared glasses ~1.2–1.4 THz). Furthermore, the scaling is similar to that observed for the simulated glasses (i.e., decreasing intensity and increasing ω_{BP} with increasing pressure), hence supporting this effect of pressure on $g(\omega)$. Now, to elucidate the nature of the BP in the simulated glasses, following Ref. [45] we normalize the frequency scale by the Debye frequency (ω_D),

$$\lim_{\omega\to 0}\frac{g(\omega)}{\omega^2}=\frac{4\pi}{nV_D^3}=\frac{3}{\omega_D^3}, \tag{13}$$

where n is the atomic number density of the glass and $V_D^3=(((1/V_L^3)+(2/V_T^3))/3$ is the average sound velocity. We also scale the reduced $g(\omega)$ according to the limit of Eq. (13). The normalized reduced $g(\omega)$ is presented in Fig. 6d, showing that the boson peak frequency and intensity largely collapse onto a single curve upon the performed normalization, at least for samples with pressures $\geq$ 10 GPa. This finding suggests that the changes in the glasses are mainly governed by the transformation of the elastic continuum [45].

Next, we compute the participation ratio (PR, see Eq. (8)) to deduce the localization of the various modes at different pressures (Fig. 7a). This analysis shows an increase in PR with increasing pressure for higher frequency, with the exception that the high frequency modes generally shift towards lower frequencies at higher pressures (Fig. 6a). Furthermore, we observe a significant fraction of low-frequency modes with a very low participation ratio (Fig. 7a). Similar modes have previously been observed in a range of both simplified computer model glasses as well as in simulations of more realistic glasses (e.g., network glasses similar to the oxide glasses in the present study)[46,47]. From these data, we quantify the relative fraction of extendons (i.e., propagons and diffusons) by counting a locon as a mode with PR< 0.15. Based on this quantification, we find an interesting trend with a transition region from ~78% of modes being extendons for the as-prepared glass to ~95% of the modes being extendons in the glass compressed at 100 GPa (Fig. 7b). This transition occurs gradually throughout the probed pressure range and levels off at around 50 GPa. Comparing this pressure dependence with that of the presented structural parameters, we note that the shape of the curve in Fig. 7b largely mimics that of the CN of oxygen and silicon (Fig. 2), suggesting that the network forming species control the degree of mode localization. To this end, we have included a plot of the correlation between CN and the fraction of extended modes in Fig. S3, showing approximate linear correlations for oxygen and silicon, but a non-linear tendency for aluminum at lower coordination numbers.

To couple the studied vibrational properties to the heat conducting properties of the CAS glass system, we first compute the second- and third-order force constants of the simulated system as it allows us to employ the recently developed quasi-harmonic Green-Kubo (QHGK) method[12,28]. In turn, this enables the computation of the contribution of each mode to the total thermal conductivity (κ). The total thermal conductivity is presented in Fig. 8a, showing a significant pressure-induced increase in κ at lower pressures (0–40 GPa) from ~1.0 to ~1.6 W m^{-1} K^{-1}, and then a smaller increase in κ from ~1.6 to ~1.7 W m^{-1} K^{-1} when the pressure increases further to 100 GPa. We note how the κ value of the as-prepared glass is close to experimental thermal conductivity of 0.954 W m^{-1} K^{-1}, which increases to 0.995 W m^{-1} K^{-1} upon hot-compression to 1 GPa in qualitative agreement with the trend found in the MD simulations. Table S1 summarizes experimental results of heat capacity and thermal diffusivity of the as-prepared and hot-compressed glasses.

Next, the modal contributions to κ as calculated from QHGK allows us to compute a cumulative κ as presented in Fig. 8b. First, we note a significant contribution from the low-frequency modes, e.g., the as-prepared glass features almost exclusively contributions from modes with frequencies below 20 THz, although the $g(\omega)$ is occupied up to nearly 40 THz (Fig. 6a). With increasing pressure, the inflection frequency of the curves in Fig. 8b increases similarly to the frequency at which κ reaches a constant value that also increases. We find that this is mainly driven by a pressure-induced increase in diffusivity across most of the modal spectrum as shown in Fig. S4. The modal κ also allows us to probe correlations with the PR. By plotting the modal κ directly as a function of the PR of each mode, we find generally that low PR modes (locons) exhibit very small modal κ, but also that PR and modal κ do not have a simple correlation (Fig. S5). The former is further supported by calculating the contributions of locons to total κ (Fig. S6), finding that extendons contribute to > 97.5% of κ in all the simulated glasses with a

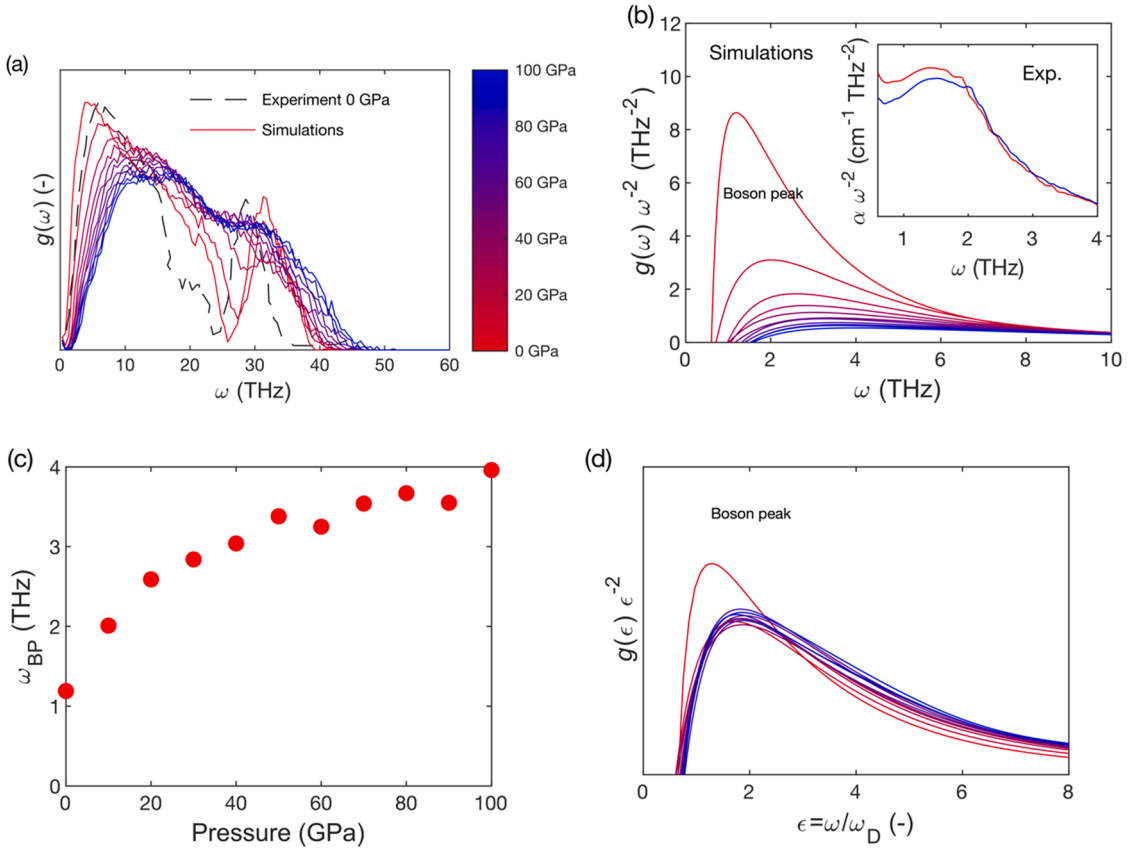

Fig. 6. (a) Vibrational density of states (VDOS) ($g(\omega)$) and (b) reduced VDOS ($g(\omega)\omega^{-2}$) of the simulated 30CaO-10Al_2O_3-60SiO_2 glasses as functions of pressure. The color bar indicates pressure (red: 0 GPa and blue: 100 GPa). The dashed line in (a) indicates experimental $g(\omega)$ from neutron scattering for a 43CaO-14Al_2O_3-43SiO_2 glass[44]. The inset in (b) shows the reduced absorption coefficient as obtained in the present study from THz time-domain spectroscopy for the experimental as-prepared 30CaO-10Al_2O_3-60SiO_2 (red) as well as the same glass after hot-compression at 1 GPa (blue). (c) The frequency of the boson peak (ω_{BP}) as a function of pressure for the simulated 30CaO-10Al_2O_3-60SiO_2 glasses from 0 to 100 GPa. (d) Reduced VDOS rescaled by the Debye frequency (ω_D) in its horizontal axis as well as by its zero frequency limit in the vertical axis (see Eq. 13).

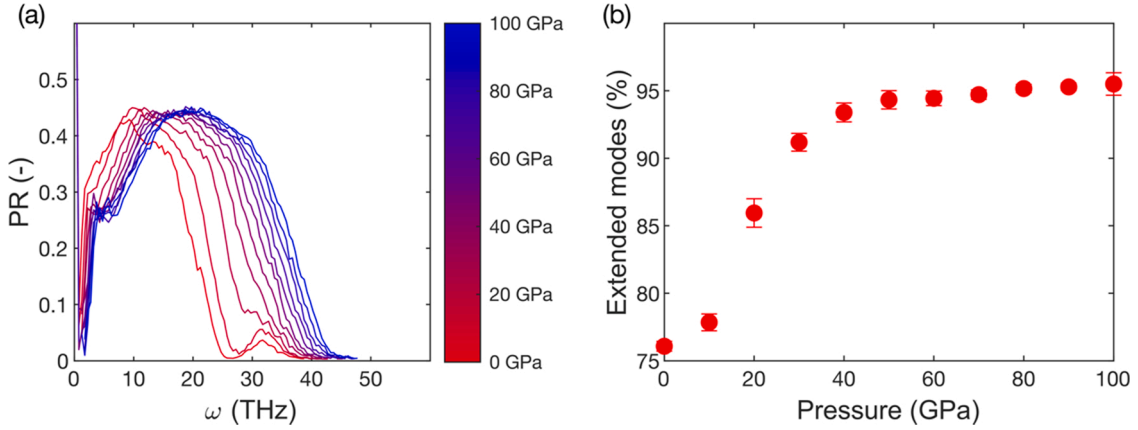

Fig. 7. (a) Frequency dependence of the participation ratio (PR) and (b) pressure dependence of the relative number of extended modes for all simulated 30CaO-10Al_2O_3-60SiO_2 glasses. The increasing pressure is seen to greatly decrease the number of localized modes in the high-frequency region.

slightly increasing contribution with increasing pressure. This tendency is significant despite how a relatively large amount of locons exist at low pressures (Fig. 7b). Furthermore, it is in good accordance with the concept that locons only have a negligible contribution to κ.

Further coupling the thermal conductivity data from Fig. 8a with the BP position from Fig. 6c provides an intriguing correlation as shown in Fig. 9a. This positive correlation between the BP and κ points to a causal relation between these quantities and although authors have previously discussed links between thermal conduction and vibrational modes linked to the BP [48–50], this, to our knowledge, is the first evidence of a direct relation between the BP and κ. Fig. 9a also includes experimental values of boson peak frequency and thermal conductivity for lithium borate glasses from literature [51,52]. Interestingly, this dataset also shows a linear trend and a similar slope to that of the studied CAS system. Another intriguing correlation is that between the BP peak position and the glass density as presented in Fig. 9b. Similar correlations of

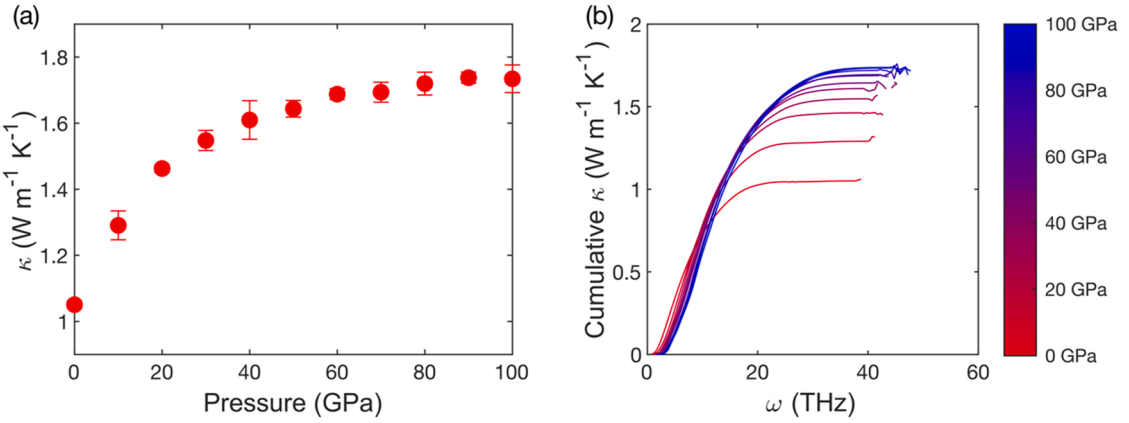

Fig. 8. (a) Total and (b) cumulative thermal conductivity (κ) as a function of pressure for the simulated 30CaO-10Al_2O_3-60SiO_2 glasses.

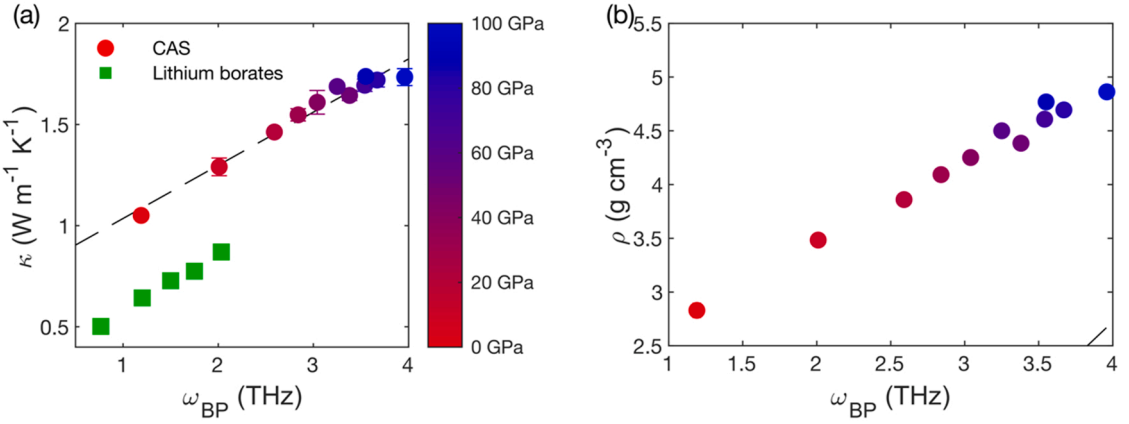

Fig. 9. (a) Total thermal conductivity (κ) as a function of the frequency of the boson peak (ω_{BP}) for the simulated 30CaO-10Al_2O_3-60SiO_2 glasses as well as for lithium borate glasses (in the 0–25 mol% Li_2O composition range) as obtained from Refs.[51,52]. (b) Frequency of the boson peak (ω_{BP}) as a function of density (ρ) of the simulated CAS glasses. The color bar indicates pressure (red: 0 GPa; blue: 100 GPa).

increasing ω_{BP} (and decreasing BP intensity) with densification have previously been inferred in the pure SiO_2 system (for both crystalline and amorphous systems) based on experimental measurements on systems with matching densities [53]. In a previous study on silicon-like material, a maximum in diffusivity at frequencies surpassing the boson peak position was observed, but the authors noted that the boson peak was coalescing with the Ioffe-Regel transition of transverse modes [50]. The latter is in agreement with previous work on computer glasses [54]. In this work, we find no immediate change of the per mode diffusivity in relation to BP frequency (see examples in Fig. S4). However, by binning the per-mode diffusivities, we find that the maximum in diffusivity shifts to higher frequencies with pressure (Fig. 10).

This shift of the maximum mode diffusivity is similar to that of the boson peak (Fig. 6c) and the frequency region is very similar (1–4 THz).

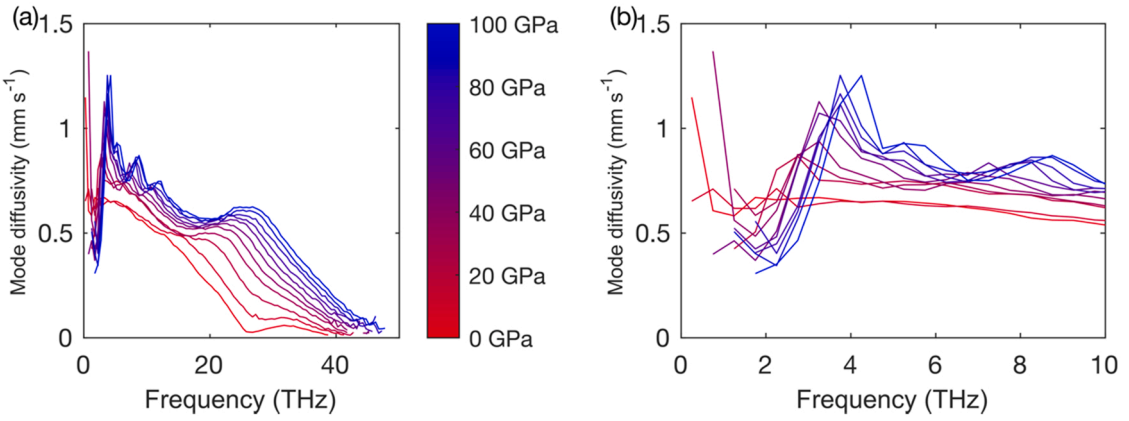

Fig. 10. (a) Full spectral range and (b) low-frequency range of binned mode diffusivities. An overall increase in diffusivity is noted as well as increasing low-frequency contribution and narrowing of the spectral region with the highest contribution to diffusivity with increasing pressure. The color bar indicates pressure (red: 0 GPa; blue: 100 GPa).

As such, we find that the boson peak and diffusivity maximum coalesce, being in contrast to the previous report on amorphous silicon-like materials [50]. However, as shown in Fig. 8b, the change of the thermal conductivity is mainly governed by changes in the higher frequency spectral region (20–40 THz). Following the results shown in Fig. 10a, this is consistent with a significant increase in diffusivity in the same spectral region. Furthermore, a similar change from low to high PR values (Fig. 7a) is found for modes in this spectral region with increasing pressure. In terms of network structure, from the partial $g(\omega)$ (Fig. S2), it is primarily the oxygen and silicon that populate this spectral region and thus likely the main atom types responsible for the significant changes of thermal conduction.

The following question then arises: what is the origin of the apparent correlation between the boson peak and contributions from higher frequency modes? This correlation could indicate that these two parameters follow the same Debye dependency. That is, as the boson peak is shown to collapse nicely by normalization with the Debye frequency, this will also be the case for thermal conductivity based on the linear correlation between these two parameters (Fig. 9a). In turn, this implies that thermal conduction, as well as the shift of the boson peak, is a basic consequence of the transformation of the elastic medium. In relation to this, one may consider the fundamental idea of the Debye model regarding how increasing Debye frequency effectively translates into a larger cutoff frequency in $g(\omega)$. To this end, it is interesting to note that the pressure increase results in higher Debye frequencies, a shift of $g(\omega)$ towards higher frequencies (Fig. 6a) and an increased participation of these modes (Fig. 7), resulting in a larger diffusivity (Fig. 10a) and ultimately increasing thermal conductivity (Figs. 8 and 9). Hence, our results suggest that the Debye behavior of the studied materials effectively governs both the low-frequency boson peak behavior and the enhancement of participating modes at higher frequencies.

4. Conclusions

We have simulated the quenching procedure of a calcium aluminosilicate glass ($30CaO\text{-}10Al_2O_3\text{-}60SiO_2$) under hydrostatic pressures ranging from 0–100 GPa and experimentally hot-compressed a glass of the same composition at 1 GPa. With increasing pressure, the coordination numbers, elastic moduli, and sound speeds increase. Further analysis of the vibrational properties shows significant changes in the vibrational density of states, corresponding to a boson peak region with an increasing boson peak frequency and decreasing intensity with increasing pressure. We validate this trend experimentally using THz time-domain spectroscopy. Extended harmonic and anharmonic lattice dynamics analysis shows that the degree of localized modes is significantly reduced with increasing pressure while the thermal conductivity is found to significantly increase from 1.0 to 1.7 $W\ m^{-1}\ K^{-1}$. We find the increase of thermal conductivity to be governed by an increase in diffusivity in the 20–40 THz spectral range, mainly governed by oxygen and silicon vibrations. Furthermore, we have found a positive correlation between the boson peak frequency and thermal conductivity, which we ascribe to a common relation to the Debye scaling of the transformation of the elastic medium.

CRediT authorship contribution statement

Søren S. Sørensen: Conceptualization, Methodology, Investigation, Formal analysis, Writing – original draft, Writing – review & editing. **Paweł P. Cielecki**: Investigation, Methodology, Writing – review & editing. **Hicham Johra**: Investigation, Writing – review & editing. **Michael Bockowski**: Investigation, Writing – review & editing. **Esben Skovsen**: Investigation, Methodology, Writing – review & editing. **Yuanzheng Yue**: Conceptualization, Writing – review & editing. **Morten M. Smedskjaer:** Conceptualization, Writing – review & editing, Supervision, Funding acquisition.

Declaration of Competing Interest

The authors declare that they have no known competing financial interests or personal relationships that could have appeared to influence the work reported in this paper.

Data Availability

Presented data and scripts underlying the simulation results are available from the corresponding author upon request.

Acknowledgments

We thank Tobias K. Bechgaard for providing the calcium aluminosilicate glass samples and CLAAUDIA at Aalborg University for access to computing power. This work was supported by the Independent Research Fund Denmark (grant no. 7017–00019).

Supplementary Material

See the supplementary material for details of physical properties of hot-compressed glasses, as well as radial distribution functions, partial vibrational density of states, mode diffusivities, and detailed thermal conductivity analysis of simulated glasses.

Appendix A. Supporting information

Supplementary data associated with this article can be found in the online version at doi:10.1016/j.mtcomm.2022.104160.

References

[1] P.B. Allen, J.L. Feldman, J. Fabian, F. Wooten, Diffusons, Locons, Propagons: Character of Atomic Vibrations in Amorphous Silicon, Philos. Mag. B. (1998).
[2] R. Peierls, Zur kinetischen Theorie der Wärmeleitung in Kristallen, Ann. Phys. 395 (1929) 1055–1101.
[3] C. Kittel, Interpretation of the thermal conductivity of glasses, Phys. Rev. 75 (1949) 972–974, https://doi.org/10.1103/PhysRev.75.972.
[4] W. Lv, A. Henry, Examining the validity of the phonon gas model in amorphous materials, Sci. Rep. 6 (2016) 37675, https://doi.org/10.1038/srep37675.
[5] H.R. Seyf, L. Yates, T.L. Bougher, S. Graham, B.A. Cola, T. Detchprohm, M.-H. Ji, J. Kim, R. Dupuis, W. Lv, A. Henry, Rethinking phonons: the issue of disorder, Npj Comput. Mater. 3 (2017) 49, https://doi.org/10.1038/s41524-017-0052-9.
[6] W. Zhou, Y. Cheng, K. Chen, G. Xie, T. Wang, G. Zhang, Thermal conductivity of amorphous materials, Adv. Funct. Mater. (2019) 1903829, https://doi.org/10.1002/adfm.201903829.
[7] P.B. Allen, J.L. Feldman, Thermal conductivity of glasses: theory and application to amorphous Si, Phys. Rev. Lett. 62 (1989) 645–648, https://doi.org/10.1103/PhysRevLett.63.2104.
[8] P.B. Allen, J.L. Feldman, J. Fabian, F. Wooten, Diffusons, locons and propagons: Character of atomic vibrations in amorphous Si, Philos. Mag. B 79 (1999) 1715–1731, https://doi.org/10.1080/13642819908223054.
[9] M. Beekman, D.G. Cahill, Inorganic Crystals with Glass-Like and Ultralow Thermal Conductivities, Cryst. Res. Technol. 52 (2017) 1700114, https://doi.org/10.1002/crat.201700114.
[10] D.G. Cahill, S.K. Watson, R.O. Pohl, Lower limit to the thermal conductivity of disordered crystals, Phys. Rev. B 46 (1992) 6131–6140, https://doi.org/10.1103/PhysRevB.46.6131.
[11] M.T. Agne, R. Hanus, G.J. Snyder, Minimum thermal conductivity in the context of diffuson-mediated thermal transport, Energy Environ. Sci. 11 (2018) 609–616, https://doi.org/10.1039/c7ee03256k.
[12] M. Simoncelli, N. Marzari, F. Mauri, Unified theory of thermal transport in crystals and disordered solids, Nat. Phys. 15 (2019) 809–813.
[13] G. Barbalinardo, Z. Chen, N.W. Lundgren, D. Donadio, Efficient anharmonic lattice dynamics calculations of thermal transport in crystalline and disordered solid, J. Appl. Phys. 128 (2020), 135104, https://doi.org/10.1063/5.0020443.
[14] A.J.H. McGaughey, A. Jain, H.Y. Kim, B. Fu, Phonon properties and thermal conductivity from first principles, lattice dynamics, and the Boltzmann transport equation, J. Appl. Phys. 125 (2019), 011101, https://doi.org/10.1063/1.5064602.
[15] Y. Zhou, A. Morshedifard, J. Lee, M.J.A. Qomi, The contribution of propagons and diffusons in heat transport through calcium-silicate-hydrates, Appl. Phys. Lett. 110 (2017), 043104, https://doi.org/10.1063/1.4975159.
[16] Y. Tian, J. Du, W. Han, X. Zu, X. Yuan, W. Zheng, Thermal conductivity of vitreous silica from molecular dynamics simulations: The effects of force field, heat flux and system size, J. Chem. Phys. 146 (2017), 054504, https://doi.org/10.1063/1.4975162.

[17] A.K. Varshneya, Fundamentals of inorganic glasses, 2013.
[18] J.E. Shelby. Introduction to Glass Science and Technology, 2nd ed., The Royal Society of Chemistry, 2005 https://doi.org/10.1039/9781847551160.
[19] A. Ellison, I.A. Cornejo, Glass substrates for liquid crystal displays, Int. J. Appl. Glas. Sci. 1 (2010) 87–103, https://doi.org/10.1111/j.2041-1294.2010.00009.x.
[20] M. Solvang, Y.Z. Yue, S.L. Jensen, D.B. Dingwell, Rheological and thermodynamic behaviors of different calcium aluminosilicate melts with the same non-bridging oxygen content, J. Non Cryst. Solids 336 (2004) 179–188, https://doi.org/10.1016/j.jnoncrysol.2004.02.009.
[21] T.K. Bechgaard, J.C. Mauro, M. Bauchy, Y. Yue, L.A. Lamberson, L.R. Jensen, M. M. Smedskjaer, Fragility and configurational heat capacity of calcium aluminosilicate glass-forming liquids, J. Non Cryst. Solids 461 (2017) 24–34, https://doi.org/10.1016/j.jnoncrysol.2017.01.033.
[22] M. Bauchy, Structural, vibrational, and elastic properties of a calcium aluminosilicate glass from molecular dynamics simulations: the role of the potential Structural, vibrational, and elastic properties of a calcium aluminosilicate glass from molecular dynami, J. Chem. Phys. 141 (2014), 024507, https://doi.org/10.1063/1.4886421.
[23] D.R. Neuville, L. Cormier, D. Massiot, Al coordination and speciation in calcium aluminosilicate glasses: Effects of composition determined by27Al MQ-MAS NMR and Raman spectroscopy, Chem. Geol. 229 (2006) 173–185, https://doi.org/10.1016/j.chemgeo.2006.01.019.
[24] M. Matsui, Molecular dynamics study of the structures and bulk moduli of crystals in the system CaO-MgO-Al_2O_3-SiO_2, Phys. Chem. Miner. 23 (1996) 345–353, https://doi.org/10.1007/BF00199500.
[25] S. Plimpton, Fast parallel algorithms for short-range molecular dynamics, J. Comput. Phys. 117 (1995) 1–19, https://doi.org/10.1006/jcph.1995.1039.
[26] M.T. Dove, Introduction to Lattice. Dynamics, 1st ed..,, Cambridge University Press, 1993.
[27] L. Pedesseau, S. Ispas, W. Kob, First-principles study of a sodium borosilicate glass-former. II. the glass state, Phys. Rev. B 91 (2015), 134202, https://doi.org/10.1103/PhysRevB.91.134202.
[28] L. Isaeva, G. Barbalinardo, D. Donadio, S. Baroni, Modeling heat transport in crystals and glasses from a unified lattice-dynamical approach, Nat. Commun. 10 (2019) 3853. https://doi.org/10.1038/s41467-019-11572-4.
[29] M.N. Svenson, T.K. Bechgaard, S.D. Fuglsang, R.H. Pedersen, A.O. Tjell, M. B. Østergaard, R.E. Youngman, J.C. Mauro, S.J. Rzoska, M. Bockowski, M. M. Smedskjaer, Composition-structure-property relations of compressed borosilicate glasses, Phys. Rev. Appl. 2 (2014), 024006, https://doi.org/10.1103/PhysRevApplied.2.024006.
[30] S. Kapoor, L. Wondraczek, M.M. Smedskjaer, Pressure-induced densification of oxide glasses at the glass transition, Front. Mater. 4 (2017) 1, https://doi.org/10.3389/fmats.2017.00001.
[31] Q. Zheng, Y. Zhang, M. Montazerian, O. Gulbiten, J.C. Mauro, E.D. Zanotto, Y. Yue, Understanding glass through differential scanning calorimetry, Chem. Rev. 119 (2019) 7848–7939, https://doi.org/10.1021/acs.chemrev.8b00510.
[32] C.G. Maier, K.K. Kelley, An equation for the representation of high-temperature heat content data, J. Am. Chem. Soc. 54 (1932) 3243–3246, https://doi.org/10.1021/ja01347a029.
[33] S.S. Sørensen, M.S. Bødker, H. Johra, R.E. Youngman, S.L. Logunov, M. Bockowski, S.J. Rzoska, J.C. Mauro, M.M. Smedskjaer, Thermal conductivity of densified borosilicate glasses, J. Non Cryst. Solids 557 (2021), 120644, https://doi.org/10.1016/j.jnoncrysol.2021.120644.
[34] P.P. Cielecki, E. Skovsen, A compact, 3D printable purge system for terahertz, Spectroscopy (2021), https://doi.org/10.5281/zenodo.5358095.
[35] J.W.E. Drewitt, S. Jahn, C. Sanloup, C. De Grouchy, G. Garbarino, L. Hennet, Development of chemical and topological structure in aluminosilicate liquids and glasses at high pressure, J. Phys. Condens. Matter 27 (2015), 105103, https://doi.org/10.1088/0953-8984/27/10/105103.
[36] A. Pakhomova, D. Simonova, I. Koemets, E. Koemets, G. Aprilis, M. Bykov, L. Gorelova, T. Fedotenko, V. Prakapenka, L. Dubrovinsky, Polymorphism of feldspars above 10 GPa, Nat. Commun. 11 (2020) 2721, https://doi.org/10.1038/s41467-020-16547-4.
[37] M. Murakami, S. Kohara, N. Kitamura, J. Akola, H. Inoue, A. Hirata, Y. Hiraoka, Y. Onodera, I. Obayashi, J. Kalikka, N. Hirao, T. Musso, A.S. Foster, Y. Idemoto, O. Sakata, Y. Ohishi, Ultrahigh-pressure form of SiO_2 glass with dense pyrite-type crystalline homology, Phys. Rev. B. 99 (2019), 045153, https://doi.org/10.1103/PhysRevB.99.045153.
[38] P. Ganster, M. Benoit, W. Kob, J.M. Delaye, Structural properties of a calcium aluminosilicate glass from molecular-dynamics simulations: a finite size effects study, J. Chem. Phys. 120 (2004) 10172–10181, https://doi.org/10.1063/1.1724815.
[39] L. Cormier, D.R. Neuville, G. Calas, Structure and properties of low-silica calcium aluminosilicate glasses, J. Non Cryst. Solids 274 (2000) 110–114.
[40] C. Crupi, G. Carini, M. González, G. D'Angelo, Origin of the first sharp diffraction peak in glasses, Phys. Rev. B. 92 (2015), 134206, https://doi.org/10.1103/PhysRevB.92.134206.
[41] R.J. Eagan, J.C. Swearengen, Effect of composition on the mechanical properties of aluminosilicate and borosilicate glasses, J. Am. Ceram. Soc. 61 (1978) 27–30.
[42] I. Ohira, M. Murakami, S. Kohara, K. Ohara, E. Ohtani, Ultrahigh-pressure acoustic wave velocities of SiO2-Al2O3 glasses up to 200 GPa, Prog. Earth Planet. Sci. 3 (2016) 18, https://doi.org/10.1186/s40645-016-0097-2.
[43] K. Aoki, T. Sakamaki, T. Ohashi, O. Ikeda, A. Suzuki, Effects of alkali and alkaline-earth cations on the high-pressure sound velocities of aluminosilicate glasses, Phys. Chem. Miner. 47 (2020) 28, https://doi.org/10.1007/s00269-020-01098-3.
[44] J. Zhao, P.H. Gaskell, L. Cormier, S.M. Bennington, Vibrational density of states and structural origin of the heat capacity anomalies in Ca3Al2Si3O12 glasses, Phys. B. 241–243 (1998) 906–908, https://doi.org/10.1016/S0921-4526(97)00750-3.
[45] A. Monaco, A.I. Chumakov, Y.Z. Yue, G. Monaco, L. Comez, D. Fioretto, W. A. Crichton, R. Rüffer, Density of vibrational states of a hyperquenched glass, Phys. Rev. Lett. 96 (2006), 205502, https://doi.org/10.1103/PhysRevLett.96.205502.
[46] E. Lerner, G. Düring, E. Bouchbinder, Statistics and properties of low-frequency vibrational modes in structural glasses, Phys. Rev. Lett. 117 (2016), 035501, https://doi.org/10.1103/PhysRevLett.117.035501.
[47] D. Richard, K. González-López, G. Kapteijns, R. Pater, T. Vaknin, E. Bouchbinder, E. Lerner, Universality of the Nonphononic Vibrational Spectrum across Different Classes of Computer Glasses, Phys. Rev. Lett. 125 (2020) 85502, https://doi.org/10.1103/PhysRevLett.125.085502.
[48] V. Lubchenko, P.G. Wolynes, The origin of the boson peak and thermal conductivity plateau in low-temperature glasses, Proc. Natl. Acad. Sci. 100 (2003) 1515–1518, https://doi.org/10.1073/pnas.252786999.
[49] W. Schirmacher, Thermal conductivity of glassy materials and the "boson peak, Europhys. Lett. 73 (2006) 892–898, https://doi.org/10.1209/epl/i2005-10471-9.
[50] Y.M. Beltukov, C. Fusco, D.A. Parshin, A. Tanguy, Boson peak and Ioffe-Regel criterion in amorphous siliconlike materials: the effect of bond directionality, Phys. Rev. E 93 (2016), 023006, https://doi.org/10.1103/PhysRevE.93.023006.
[51] S. Kojima, V.N. Novikov, M. Kodama, Fast relaxation, boson peak, and anharmonicity in Li_2O-B_2O_3 glasses, J. Chem. Phys. 113 (2000) 6344–6350, https://doi.org/10.1063/1.1309530.
[52] S.S. Sørensen, H. Johra, J.C. Mauro, M. Bauchy, M.M. Smedskjaer, Boron anomaly in the thermal conductivity of lithium borate glasses, Phys. Rev. Mater. 3 (2019), 075601, https://doi.org/10.1103/PhysRevMaterials.3.075601.
[53] A.I. Chumakov, G. Monaco, A. Fontana, A. Bosak, R.P. Hermann, D. Bessas, B. Wehinger, W.A. Crichton, M. Krisch, R. Rüffer, G. Baldi, G. Carini, G. Carini, G. D'Angelo, E. Gilioli, G. Tripodo, M. Zanatta, B. Winkler, V. Milman, K. Refson, M.T. Dove, N. Dubrovinskaia, L. Dubrovinsky, R. Keding, Y.Z. Yue, Role of disorder in the thermodynamics and atomic dynamics of glasses, Phys. Rev. Lett. 112 (2014), 025502, https://doi.org/10.1103/PhysRevLett.112.025502.
[54] H. Shintani, H. Tanaka, Universal link between the boson peak and transverse phonons in glass, Nat. Mater. 7 (2008) 870–877, https://doi.org/10.1038/nmat2293.